Enhanced photonic spin Hall shift and scattering efficiency through chiral nanoparticles

HAO ZHANG, AIZAZ KHAN, ZEESHAN AHMAD, LEI GAO, 1,2,4
ANDREY NOVITSKY, DYADONG XU, DAND DONGLIANG GAO 1,5

Abstract: The photonic spin Hall effect, arising from the spin-orbit interaction of light, has attracted rapt scientific interest owing to its applicability. Due to the limited strength of the spin-orbit interaction, the resulting photonic spin Hall shift (PSHS) is very small. In addition, the low scattering intensity hinders the applicability of the PSHS in higher-dimensional systems. Here, we explore the effect of the chirality of the particle on the far-field PSHS and the scattered intensity. We demonstrate that the chiral particle strongly supports quasi-dual symmetry when the handedness of the incident wave and the sphere match, in contrast to unmatched handedness. Under dual transformation, the spin-orbit interaction is amplified, resulting in enhanced PSHS with a characteristic redshift. Meanwhile, the far-field scattering intensity is optimized without changing the geometry of the particle. The strong spin-orbit interaction in the near-field arises due to the optical singularities in the far-vicinity, which leads to a large effective transverse force. Our results not only provide a route to tune the PSHS and scattering efficiency but might have the potential to characterize the degree of handedness of the nanoparticle.

© 2025 Optica Publishing Group under the terms of the Optica Open Access Publishing Agreement

Introduction

Light has an inherent spin angular momentum (SAM) and orbital angular momentum (OAM) [1]. These dynamic properties become coupled, known as the spin-orbit interaction (SOI) of light, when the light is focused or scattered [2]. SOI is the result of the conservation of angular momentum and is inevitable during the scattering of electromagnetic waves [1–3]. This SOI in the near-field can lead to a spin-dependent wavelength scale shift in the far-field. Akin to the classical Hall effect, the photonic spin Hall effect (PSHE) demonstrates a transverse polarization effect with a refractive index gradient replacing the role of the electric potential gradient [4,5]. While the photonic spin Hall shift (PSHS) is very small, it has been a core of scientific interest for the past couple of decades due to its wide range of applications such as edge detection [6–8] and precession measurement [9,10].

The photonic spin Hall effect is closely associated with the two types of geometrical phase, i.e., the Rytov-Vladimirskii-Berry phase and the Pancharatnam-Berry phase [11,12], which arise as a consequence of the variation in propagation direction and polarization state, respectively. These two geometric phases provide a unified description of the PSHS. Nevertheless, PSHS resulting from the limiting strength of SOI is minuscule; it requires the application of specialized approaches to be detected, such as quantum weak measurement or multiple reflections [13–15]. The quest so far is to amplify the SOI to enhance the PSHS, which has resulted in practical applications at

¹School of Physical Science and Technology, Soochow University, Suzhou 215006, China & Jiangsu Key Laboratory of Frontier Material Physics and Devices, Soochow University, Suzhou 215006, China ²School of Optical and Electronic Information, Suzhou City University & Suzhou Key Laboratory of Biophotonics & Jiangsu Key Laboratory of Biophotonics, Suzhou 215104, China

³Belarusian State University, Nezavisimosti Avenue 4, 220030 Minsk, Belarus ⁴leigao@suda.edu.cn

⁵dlgao@suda.edu.cn

planar interfaces [16]. The enhancement of PSHS in parallel dimensions [17–19] can be obtained at certain angles, like Brewster's and surface plasmon resonance angles [20–22]. In these cases, the enhancement of PSHS is achieved by effectively suppressing the Fresnel's coefficient of incident polarization while preserving that of another linear polarization [23]. However, there is a caveat: at these angles, the efficiency of PSHS is small, i.e., not all incoming photons undergo spin splitting. Recently, this dilemma has been resolved by engineered metasurfaces [24,25], which provides unprecental control over the PSHS with high efficiency [26]. In close analogy, for a spherically symmetric refractive index gradient [27], the PSHS has recently been shown to reach several wavelengths by implementing particles with electromagnetic dual symmetry [28,29]. Such scatterers preserve the helicity of the incident light [30], giving rise to strong SOI in the near-field and enhancing the PSHS in the far-field. Unfortunately, the wavelength-scale nature of the PSHS and low scattering intensity make it challenging to detect PSHS directly. While it is highly desirable to achieve high scattering intensity with enhance PSHS [31], the associated Kerker conditions leads to vanishingly small intensity at the angle of enhance PSHS.

Chirality is ubiquitous in nature and is characterized by different optical responses of enantiomers for incident light with different helicity [32]. These chiroptical effects can be quantified through circular dichroism [33]. However, quantitatively ranking the nanoparticles based on their chiral response is still a problem of concern [34]. Recently, the direct observation of SOI in the form of chiroptical signals has been demonstrated [35]. The chirality of the particle or the surrounding medium can influence the coupling of polarization and spatial degree of freedom. For quasi-anti dual chiral sphere, the strong SOI favors the enhancement of PSHS [36]. However, it is still challenging to find an exact anti-dual sphere [37]. Moreover, morphology optimization of dual nanoparticles promises enhanced scattering intensity as that of the spherical nanoparticle [31], by overlapping the electric and magnetic dipoles at their resonances. However, the enhancement of both PSHS and the scattering efficiency has yet to be realized simultaneously for a single spherical nanoparticle, restricting the practicality of the PSHS at the scale of the single spherical nanoparticle.

Here, we extend this idea to a chiral quasi-dual particle. By introducing the chirality parameter, we demonstrate that it not only allows tuning the duality of the spherical nanoparticle but, more importantly, enhances the scattering intensity without changing the morphology. When the handedness of the chiral sphere and the incident light are the same, the PSHS is enhanced as well. Moreover, we explore the strong SOI in the near-field by analyzing the spin and orbital momentum densities. Due to the presence of optical singularities in the far-vicinity of the scatterer, the effective transverse force survives in a longer vicinity, which leads to a strong deviation of streamlines and enhanced PSHS. Our results might contribute to characterizing the chiral handedness and the degree of chirality of a single nanoparticle.

2. Theoretical background

We consider a chiral spherical nanoparticle with its radius a, permittivity ε_c and permeability μ_c , which is illuminated by the incident light on the z-axis, as illustrated in Fig. 1. The electromagnetic response of a chiral medium is defined by its constitutive relations. In what follows, we adopt the Condon-Rosenfeld constitutive relations in terms of electric **E** and magnetic **H** fields [38]

$$\mathbf{D} = \varepsilon_c \mathbf{E} + i\kappa \sqrt{\varepsilon_0 \mu_0} \mathbf{H},$$

$$\mathbf{B} = \mu_c \mathbf{H} - i\kappa \sqrt{\varepsilon_0 \mu_0} \mathbf{E},$$
(1)

where ε_0 (μ_0) is the free space permittivity (permeability) and κ is the chirality parameter. We define the handedness of the chiral particle in accordance with the sign of chirality parameter κ . For brevity, κ is positive for the right-handed sphere and negative for the left-handed sphere. By implementing the Mie scattering theory [39], the scattered electric \mathbf{E}^s and magnetic \mathbf{H}^s fields

from a chiral sphere can be obtained as follows [40].

$$\mathbf{E}^{s} = E_{0} \sum_{n=1}^{\infty} \sum_{m=-n}^{n} \left[A_{mn}^{s} \mathbf{M}_{mn}^{(3)}(\mathbf{r}, k) + B_{mn}^{s} \mathbf{N}_{mn}^{(3)}(\mathbf{r}, k) \right],$$
(2)

$$\mathbf{H}^{s} = \frac{kE_{0}}{i\omega\mu} \sum_{n=1}^{\infty} \sum_{m=-n}^{n} [A_{mn}^{s} \mathbf{N}_{mn}^{(3)}(\mathbf{r}, k) + B_{mn}^{s} \mathbf{M}_{mn}^{(3)}(\mathbf{r}, k)],$$
(3)

where the superscript "s" accounts for the scattered field, E_0 is amplitude, $k = \omega(\varepsilon_0 \mu_0)^{1/2}$ is the wave number of the incident wave, A^s_{mn} and B^s_{mn} are the scattering coefficients. By implementing the boundary conditions [41] at the surface (r = a) of the chiral sphere, the scattering coefficients A^s_{mn} and B^s_{mn} can be obtained as

$$A_{mn}^{s} = A_{n}^{sa} a_{mn}^{ip} + A_{n}^{sb} b_{mn}^{ip}, B_{mn}^{s} = B_{n}^{sa} a_{mn}^{ip} + B_{n}^{sb} b_{mn}^{ip},$$
(4)

where, the superscripts "i" and "p" indicate the incident field and it's polarization, respectively. The expressions for A_n^{sa} , A_n^{sb} , B_n^{sa} , B_n^{sb} and the expansion coefficients a_{mn}^{ix} and b_{mn}^{ix} for linearly x-polarized incident light are given in the appendix A. Whereas, for the y-polarized incident wave, the expansion coefficients are related to a_{mn}^{ix} and b_{mn}^{ix} through $a_{mn}^{iy} = -ib_{mn}^{ix}$ and $b_{mn}^{iy} = -ia_{mn}^{ix}$. Illuminating a particle with a linearly polarized light results in zero transverse displacement of the particle [16] because of null spin flow. Nevertheless, for such spin-less beams, the optical mirages can still arise as a result of interference, provided that the particle does support both electric and magnetic response [42]. The eigenmodes of PSHS shift are purely the right circular polarization (RCP) and left circular polarization (LCP) states [43]. Hereafter, we turn to circular polarization, for which the expansion coefficients can be obtained from the superposition of two orthogonally vibrating linearly polarized waves. The expansion coefficients of RCP plane wave $\mathbf{E}^{iR} = E_0 e^{ikz} (\hat{x} + i\hat{y})$ can be expressed as the combination of a_{mn}^{ix} and b_{mn}^{ix} [44]:

$$a_{mn}^{iR} = b_{mn}^{iR} = \frac{1}{\sqrt{2}} (a_{mn}^{ix} + b_{mn}^{ix}), \tag{5}$$

where the coefficient $1/\sqrt{2}$ is due to the normalization of the electric field. Similarly, for the LCP wave with the field $\mathbf{E}^{iL} = E_0 e^{ikz} (\hat{x} - i\hat{y})$, the expansion coefficients can be explicitly obtained as

$$a_{mn}^{iL} = -b_{mn}^{iL} = \frac{1}{\sqrt{2}} (a_{mn}^{ix} - b_{mn}^{ix}). \tag{6}$$

At this stage, one can obtain the scattered electric and magnetic fields using the scattered field coefficients. The PSHS for a spherical particle can be obtained from the Poynting vector $\mathbf{S}(\mathbf{r})$ of the scattered field. In spherical coordinates, the radial component $\mathbf{S}(\mathbf{r})$ governs the energy flow along the propagation direction of outgoing spherical waves, while the angular and azimuthal components define the transversal energy flow. PSHS arises as a transverse displacement in the perceived position of the particle, as illustrated in Fig. 1. The azimuthal component determines the amplitude of the PSHS [45]

$$\Delta_{\rm SH} = \lim_{r \to \infty} r \left(-\frac{S_{\varphi}}{|S_r|} \right) \hat{\varphi},\tag{7}$$

where the S_{φ} and S_r are the azimuthal and radial components of the Poynting vector $\mathbf{S}(\mathbf{r})$ of the scattered field.

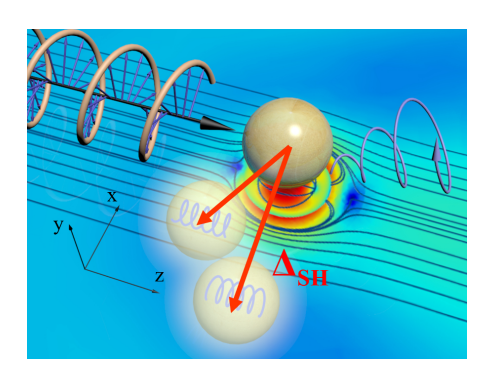


Fig. 1.: A spherical chiral particle is illuminated by a circularly polarized wave of defined helicity. In the near-field, the spin-orbit interaction results a shift in the perceived location of the particle in the far-field, as represented by the red arrows. In the view of the detector, due to the intrinsic particle chirality, the magnitude of Δ_{SH} is different for illumination with different circular polarization.

3. Duality and photonic spin Hall shift

For numerical results, we consider a chiral sphere of radius a=131 nm and the permittivity (silicon) $\varepsilon_c=3.55^2$, illuminated by a circularly polarized plane wave with wavelength λ [27]. Although optimizing the refractive index of the surrounding medium can support a lower value of the chirality parameter for enhancing the PSHS [36], we assume the sphere in the air for simplicity. Without the loss of generality, we assume the incident light as RCP throughout the results. To clearly observe the variation of the PSHS with respect to both incident wavelength and chirality parameter, we show the maximum value of the PSHS along the full range of scattering angles. As illustrated in Fig. 2, while the peak value of PSHS is enhanced for the right-handed chiral particle, it undergoes a redshift for both right (κ >0) and left-handed (κ <0) chiral spheres.

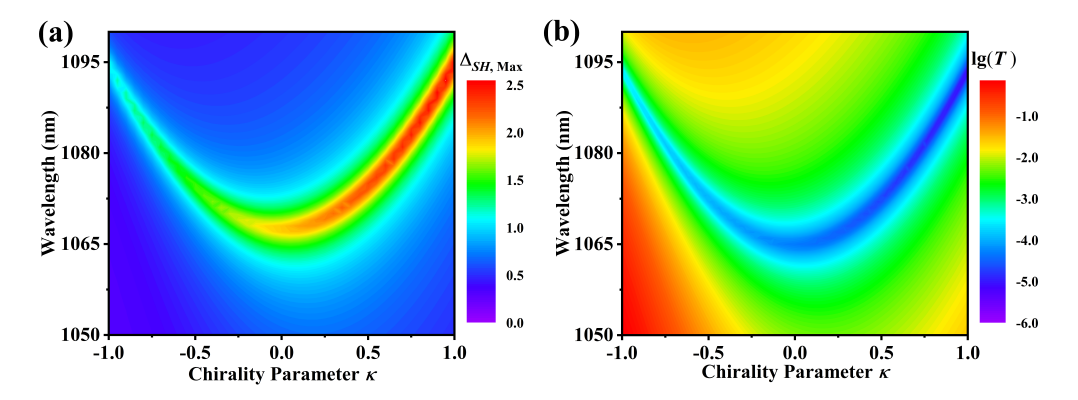


Fig. 2. Symmetry analysis and Photonic spin Hall shift: (a) Maximum Photonic spin Hall shift (PSHS) and (b) the variation of the transfer function against the chirality parameter and incident wavelength. For positive chirality parameter, the transfer function approaches zero and the PSHS is enhanced.

At this stage, we perform a symmetry analysis of the chiral particle, as shown in Fig. 2(b). A dual spherical particle can be defined as one which preserves the helicity of incident light. It satisfies the first Kerker conditions, i.e., $a_j(x) = b_j(x) \forall j, x$ when $\mu_r = \varepsilon_r$ [37]. For a chiral spherical particle, the cross-coupling modifies the scattering coefficients. While it is hard to

achieve the exact first Kerker condition, it is reasonable to evaluate the dual response of the chiral particle by the closed analytical-expression in Ref. [46] or alternatively from the ratio of energy scattered with opposite helicity, which can be quantified using the transfer function $T = w_{-p}^{sca}/w_p^{sca}$ [47]. Here w_{-p}^{sca} is the energy scattered with opposite helicity, while w_p^{sca} is the fraction of energy scattered with the same helicity as that of the incident wave. The transfer function can be simplified as

$$T = \frac{\sum_{n=1}^{\infty} \frac{n^2(n+1)^2}{2n+1} \left| A_{1n}^s - B_{1n}^s \right|^2}{\sum_{n=1}^{\infty} \frac{n^2(n+1)^2}{2n+1} \left| A_{1n}^s + B_{1n}^s \right|^2}.$$
 (8)

A direct analysis shows that the transfer function T approaches zero if the scattering coefficients are equal in magnitude and phase. In this case, the denominator w_p^{sca} is dominant and scattered energy exhibits the same helicity as the incident light [36,37]. It is to be noted that, if the scattering coefficients are out of phase and equal in magnitude (second Kerker condition), optimal backward light scattering is achieved, but anti-duality does not occur unless the extinction is zero [48]. The enhanced maximum of PSHS corresponds to the quasi-dual symmetry cases, i.e., the transfer function approaches zero, as shown in Fig. 2(b). Interestingly, when the handedness of the incident wave and the chiral particle are the same, the chiral particle exhibits quasi-dual symmetry more prominently. That is, the interaction of incident wave helicity and the intrinsic chirality of the sphere can optimize the quasi-dual symmetry, leading to the enhancement of PSHS when the handedness matches. It is worth to note that the transfer function for LCP incident light varies as a results of different scattering coefficients and the quasi-dual response is more prominent as one move towards the negative chirality (not shown here). The corresponding results can be obtained for LCP incident light by using the transfer function given in appendix B.

So far, we have demonstrated that PSHS is enhanced when the circular handedness of the incident light matches that of the chiral particle. Under such conditions, the particle behaves as quasi-dual. The quasi-dual response is associated with the first Kerker condition, which results in pronounced forward scattering. In the following section, we show that for larger values of the chirality parameter, the scattering coefficients of the chiral sphere overlap at higher values, leading to optimize the scattering intensity along with enhance PSHS.

4. Scattering Intensity

The PSHS is typically amplified at specific scattering angles, which coincide with vanishing scattering intensity. In the case of nanoparticles, this dilemma between the PSHS and the far-field scattering intensity arises as a result of highly directional scattering as a consequence of the first Kerker conditions. The PSHS expressed in Eq. (7) can be rewritten in terms of the far-field scattering intensity $I(\theta)$ described in appendix B, as follows

$$\Delta_{\text{SH}} = -\frac{\sqrt{2}\sigma\sin\theta}{2k}E_0^2 \frac{Re\left[\sum_{n=1}^{\infty}\sum_{m=-n}^{n}C_n((-1)^{n+1}B_{mn}^s\pi_{mn}\cdot S_1^* + \sigma S_2\cdot (A_{mn}^s\pi_{mn})^*)\right]}{I(\theta)}.$$
 (9)

From Eq. (9), it can be seen that an inverse relationship exists between the PSHS and the scattering intensity. Therefore, low scattering intensity is inherent to enhanced PSHS and achieving a simultaneous enhancement of both PSHS and the scattering intensity is a significant challenge. The scattering intensity is proportional to the scattering coefficients, whereas the enhanced PSHS requires equal scattering coefficients in phase. Thus, in order to enhance PSHS and the scattered intensity simultaneously, the scattering coefficients must overlap at their resonances. However, this requires breaking the spherical geometry of the particle [31].

Interestingly, the extent of the chiral handedness of the particle naturally tunes the overlap of scattering coefficients to higher values with characteristic redshift, which does not require breaking the spherical geometry and overlapping scattering coefficients exactly at their resonances. In Fig. 3, we demonstrate that the interplay between the chiral handedness and the helicity of the incident wave not only enhances PSHS with a redshift (Fig. 3(a)) but also optimizes the corresponding scattering intensity. To show this, we obtained the results for PSHS and the corresponding far-field scattering intensity for various values of the chirality parameter κ , as illustrated in Fig. 3(b).

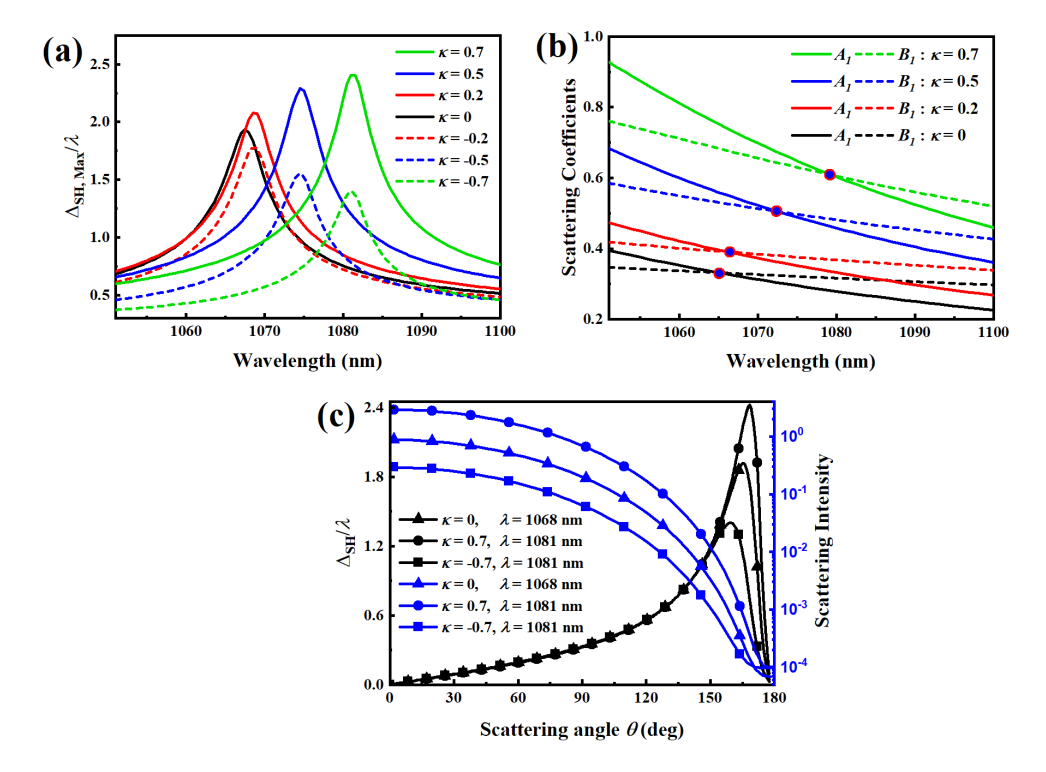


Fig. 3. Handedness matching induced simultaneous enhancement photonic spin Hall shift and scattering intensity: (a) Maximum photonic spin Hall shift (PSHS) versus incident wavelengths for various chirality parameters. Maximum PSHS shift undergoes a redshift as the chirality of the sphere is varied. (b) Scattering coefficients versus wavelength. The scattering coefficients overlap at higher values for positive chirality parmeter. (c) Scattering intensity and PSHS for chiral and achiral ($\kappa = 0$) spherical particles with scattering angles

On the one hand, it enhances the PSHS with redshift, while on the other hand, it enhances the scattering intensity, provided that the handedness of the particle and the incident light are the same. It is worth noting that the same is true for LCP incident light and left-handed sphere, with the only difference being the sign of the shift (not shown here). This means that the chirality offers another degree of freedom to manipulate the scattering intensity, similar to geometry optimization. This is an essential result of the current work, where the scattering intensity at the resonance of PSHS and the PSHS are simultaneously enhanced and optimized for a spherical scatterer without changing the morphology, as shown in Fig. 3(c). Although, the simultaneous enhancement of PSHS and the scattering intensity is theoretically achieved with large positive chirality parameter, yet high-index chiral particle with large value of chirality parameter (κ >0.2) is challenging to synthesize. While the enhancement of the scattering intensity is related to the

overlap of the scattering coefficients with relative higher values, the origin of the enhance PSHS is relied on the extent of SOI in the near-field, as demonstrated in the following sections.

5. Near-field spin-orbit interaction

In this section, we discuss the enhancement of the PSHS based on the near-field SOI. The enhancement of the PSHS indicates that the interaction of chirality between the sphere and the field could influence the transformation between SAM and OAM. Henceforth, we will focus on the trend followed by the PSHS for various chirality parameters in Fig. 3(c). We analyze the resonance that appears in PSHS in the backscattered direction. This resonance can be correlated with the measure of the differential attenuation and phases of orthogonal polarization states, i.e., diattenuation $d(\theta)$ and retardance $\delta(\theta)$, which are defined in terms of elements of the scattering matrix as [28,49]

$$d(\theta) = \frac{|S_2(\theta)|^2 \cos^2(\theta) - |S_1(\theta)|^2}{|S_2(\theta)|^2 \cos^2(\theta) + |S_1(\theta)|^2},$$
(10)

and

$$\delta(\theta) = \cos^{-1} \left[\frac{Re[S_2^*(\theta)S_1(\theta)]}{|S_2(\theta)| |S_1(\theta)|} \right].$$
 (11)

 $|d(\theta)|=1$ corresponds to a complete transformation of SAM to OAM [45]. The local maxima of the PSHS at the backscattered direction in Fig. 3(c) align with the maxima of $d(\theta)$ in Fig. 4(a), for the respective chirality parameters. Note that, at $\theta=\pi/2$ the diattenuation $d(\theta)=-1$ is due to the parallel alignment of the detector with the xz-plane, strictly it does not correspond to a strong SOI [28]. The spin flow is dependent on the chirality parameter. A more abrupt change in the relative phase of the scattered light arises for a right-handed sphere ($\kappa=0.7$), as compared to an achiral ($\kappa=0$) and a left-handed chiral sphere ($\kappa=-0.7$), which can be evaluated from the slope of the retardance $d\delta(\theta)/d\theta$. The abrupt change in retardance for $\kappa=0.7$ backscattered angle are associated with enhanced PSHS, while the coincidence of the peak of diattenuation with the peak of PSHS shows partial transformation of SAM to OAM at the backscattered direction.

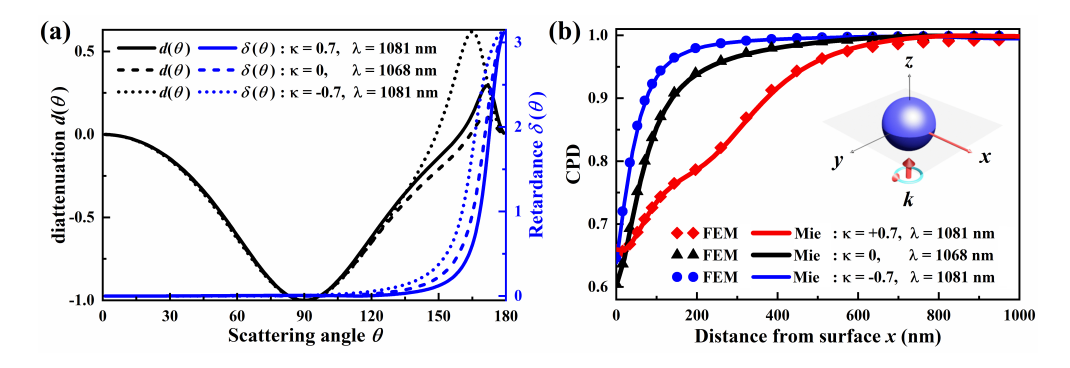


Fig. 4. Diattenuation, retardance and near-field polarization analysis: (a) Diattenuation $d(\theta)$ and retardance $\delta(\theta)$ as a function of scattering angle θ for various incident wavelength and chirality parameters. (b) Circular polarization degree from the surface of the particle along the increasing spatial x-coordinate for right, left-handed and achiral particles at various wavelengths.

We analyzed the circular polarization degree (CPD) around the nanoparticle for various cases using Mie theory and the finite element method (FEM). The CPD is defined as CPD = $|\varepsilon_0 \mathbf{E}^* \times \mathbf{E} + \mu_0 \mathbf{H}^* \times \mathbf{H}|/(\varepsilon_0 |\mathbf{E}|^2 + \mu_0 |\mathbf{H}|^2)$. A complete transformation from SAM to OAM will result in CPD = 0. In the near-field, the CPD drops to a minimum value for all cases and

approaches unity as the distance from the surface of the sphere is increased. The rapid drop in the CPD in the vicinity of the particle indicates that the SAM of light is transformed to OAM in the vicinity of the spherical particle [50], where strong SOI arises. This result is in agreement with the partial transformation as that of the diattenuation $d(\theta)$ in Fig. 4(a). What is more, this SOI can be spatially regulated by the chirality parameter, as shown in Fig. 4(b). The CPD gradually approaches the maximum value when the handedness of the incident wave and the chiral sphere are identical. That is, the spin flow extends to the far-vicinity of the chiral sphere, as we shall also show in Fig. 5 from the OMD and SAM distribution. To understand the effect of the chirality of the sphere on the near-field SOI, the Dirac form of Maxwell's equations can be introduced as, $c(\hat{\alpha} \cdot \hat{p})\Psi + \hat{\beta}V\Psi = i\partial\Psi/\partial t$ [50,51]. Here c is the speed of light propagating in vacuum, $\hat{\alpha}$ and $\hat{\beta}$ are four Dirac matrices (\hat{a}_i , i = 1, 2, 3), Ψ is the wave function formed by electric and magnetic fields, that is, $\Psi = (4\omega)^{-1/2} [(\varepsilon_0)^{1/2} \mathbf{E}, (\mu_0)^{1/2} \mathbf{H}]^T, \hat{\boldsymbol{p}} = -i \nabla$ is the canonical momentum operator, whereas V is the optical potential induced by dielectric medium [50]. The optical potential inside a non-magnetic achiral particle can be written as $\omega(1-\varepsilon)$ while outside the sphere $\omega(1-\varepsilon_m)$. For a chiral sphere, the cross-coupling modifies the potential inside the particle with additional non-zero off-diagonal elements as,

$$V = \omega \begin{pmatrix} 1 - \varepsilon & -i\kappa\sqrt{\varepsilon_0/\mu_0} \\ i\kappa\sqrt{\mu_0/\varepsilon_0} & 1 - \mu \end{pmatrix}. \tag{12}$$

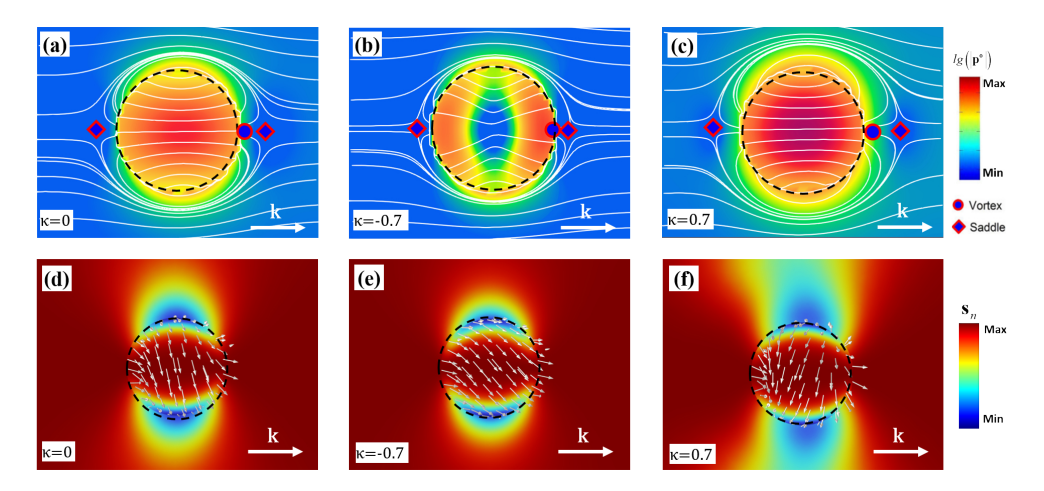


Fig. 5. Near-field spin-orbit interaction: Orbital momentum density streamlines for incident right circularly polarized light on (a) achiral ($\kappa = 0$), (b) left-handed chiral ($\kappa < 0$) and (c) right-handed chiral ($\kappa > 0$) sphere. The streamlines are projected to a plane parallel to the incident direction and contain the center of the sphere. The circles and squares represent vortex and saddle singularities, respectively. The white arrow shows the direction of the wave vector of the incident wave. (d), (e), and (f) are the normalized spin angular momentum densities $\mathbf{s_n}$ (xz-plane distribution). The white arrow indicates the direction of $\mathbf{s_n}$ near the surface of the particle. The parameters are the same as those of Fig. 4.

This potential can be obtained by putting the constitutive relations of the chiral medium in Maxwell's equations. It reduces to that of an achiral sphere [50] when there is no chirality $(\kappa=0)$. The gradient of this optical potential V mediates the SOI of light, which arises at the interface between the sphere and medium. Orbital momentum density (OMD) is defined by the expectation value $\langle \Psi | \hat{p} | \Psi \rangle$. It can be used to characterize the trajectory of photons from which the geometric phase and the effective transverse force can be understood, as we will show in

Fig. 6. The definition of OMD is as follows [49,52].

$$\mathbf{p}^o = (4\omega)^{-1} Im \left[\varepsilon_0 \mathbf{E}^*(\nabla) \mathbf{E} + \mu_0 \mathbf{H}^*(\nabla) \mathbf{H} \right]. \tag{13}$$

Similarly, the local spin angular momentum density (SMD) s can be defined by $\langle \Psi | \hat{\alpha} | \Psi \rangle$.

$$\mathbf{s} = (4\omega)^{-1} Im \left[\varepsilon_0 \mathbf{E}^* \times \mathbf{E} + \mu_0 \mathbf{H}^* \times \mathbf{H} \right]. \tag{14}$$

Compared to \mathbf{p}^o , the Poynting vector $\mathbf{S}(\mathbf{r})$ corresponds to the total momentum density [53] containing the contribution of non-energy transport components, i.e. SMD contributions $\mathbf{p}^s = (1/2)\nabla \times \mathbf{s}$ [52]. Thus, Poynting vector $\mathbf{S}(\mathbf{r})$ is not suitable to characterize the trajectory of photons. Contrary to this, the OMD is associated with the trajectory of photons [50].

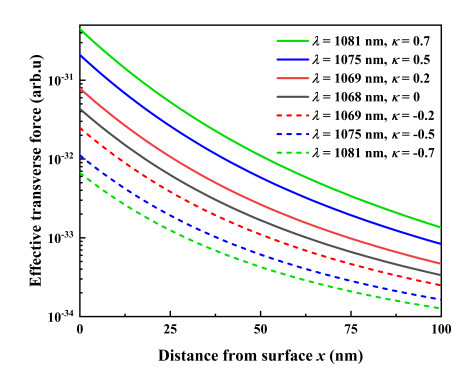


Fig. 6. Chirality dependent transverse force: Demonstration of the effective transverse force as a function of the distance from the surface of the particle in the x-direction for various chirality parameters and the incident wavelengths.

Figure 5 demonstrates the SOI regarding the interplay of the incident wave and material intrinsic chirality on the basis of OMD streamlines. We analyzed different cases for an incidence of wave in a pure state of polarization, as shown in Fig. 5. The geometric phase gradient of the scattered light allows comprehension of the PSHS [54]. SOI is mediated as a consequence of the optical potential gradient encountered by light, whose strength can be qualitatively interpreted by the extent of bending OMD streamlines. In all cases (achiral, left-handed and right-handed particles), the streamlines exhibit singularities in front as well as in the back of the scatterer, which captures the incident OMD streamlines and redirects them while accumulating geometric phase and results in a near-field strong SOI. However, the optical singularities lie relatively far from the surface of the particle, i.e., at the far-vicinity, provided that the handedness of the particle and the incident light match. The cross-coupling of chirality effectively increases the refractive index of the particle, leading to the coupling of SAM and OAM to a relatively longer spatial vicinity. Such strong SOI appears in the near-field high refractive index nanoparticle, which satisfies quasi-dual symmetry and supports optical saddle singularity [28] and optical vortex [29].

The corresponding SMD also indicates the SOI in the near-field. Figure 5(d-f) is the normalized SMD, i.e., $\mathbf{s_n} = (\omega/\mathbf{w}_{inc})\mathbf{s}$ in the xz-plane, where the white arrows show the direction of the spin angular momentum on the surface of the nanoparticle. SMD is minimal near the surface, which is in agreement with Fig. 4(b). Compared to achiral and left-handed chiral spheres, the SMD gradually approaches a maximum value and extends to the far-vicinity of the surface, as shown in Fig. 5(f).

The bending of streamlines in real space is associated with the evolution of the OMD in *k*-space. The diversion of the OMD from the original trajectory is a consequence of an effective transverse

force due to the Berry connection. Within a particular segment $(\mathbf{p}_i^o - \mathbf{p}_j^o)$, the effective force is proportional to the change in OMD streamlines $d\mathbf{p}^o$ and is given as $d\mathbf{p}^o \times \mathbf{p}^o$ [50]. Although the geometric phase can be defined in parameter space, for the sake of brevity, we demonstrate the resulting transverse force $d\mathbf{p}^o \times \mathbf{p}^o$ in real space. The transverse force is maximum near the surface for all cases and decays rapidly away from the particle, as shown in Fig. 6. However, due to the presence of the singularities in the far-vicinity of the scatterer (see Fig. 5(a, b, c)), the force is stronger and survives to the far-vicinity when the handedness is matched. The photons follow a twisted trajectory and result in enhanced PSHS in the far-field. OMD streamlines show that as one moves along the chirality axis from -1 to 1, the distortion of the streamline becomes more intense, and the coupling of SAM and OAM extends to far-vicinity. Consequently, the associated PSHS are enhanced for the right-handed cases (κ >0). Then, the increased maxima of PSHS is fully explained by the effective transverse force and the corresponding near-field singularity of OMD.

6. Conclusion

Based on generalized Mie theory, we study the influence of chirality on the photonic spin Hall shift (PSHS) from the chiral spheres. The interplay of handedness of incident light and nanoparticle tunes the quasi-dual symmetry of the particle, which can enhance PSHS and the scattered intensity, simultaneously. The singularity of orbital momentum density in the near-field shows that the spin-orbit interaction is tuned by the chirality of the nanoparticles. The long-range spin-orbit interaction leads to a relatively larger transverse force on photons, resulting in enhanced far-field PSHS. Our results can pave the way for characterizing the chirality of the nanoparticle and might be beneficial for direct observation of the spin-orbit interaction of light.

Appendix A

The incident electric \mathbf{E}^{ip} and magnetic \mathbf{H}^{ip} fields can be expressed in terms of spherical vector wave functions (SVWFs) as [40,41]

$$\mathbf{E}^{ip} = E_0 \sum_{n=1}^{\infty} \sum_{m=-n}^{n} \left[a_{mn}^{ip} \mathbf{M}_{mn}^{(1)}(\mathbf{r}, k) + b_{mn}^{ip} \mathbf{N}_{mn}^{(1)}(\mathbf{r}, k) \right], \tag{15}$$

$$\mathbf{H}^{ip} = \frac{kE_0}{i\omega\mu} \sum_{n=1}^{\infty} \sum_{m=-n}^{n} [a_{mn}^{ip} \mathbf{N}_{mn}^{(1)}(\mathbf{r}, k) + b_{mn}^{ip} \mathbf{M}_{mn}^{(1)}(\mathbf{r}, k)], \tag{16}$$

where, a_{mn}^{ip} and b_{mn}^{ip} are expansion coefficients of the incident field. The incident wave can exhibit any polarization. For simplicity, we represent the incident polarization of the fields by the superscript ip in the above equations. Based on Bohren's method, an arbitrary wave inside a chiral sphere can be decomposed into a left circular polarized (LCP) wave with wave number $k_1 = \omega[(\varepsilon_c \mu_c)^{1/2} - \kappa(\varepsilon_0 \mu_0)^{1/2}]$ and a right circular polarized (RCP) wave with wave number $k_2 = \omega[(\varepsilon_c \mu_c)^{1/2} + \kappa(\varepsilon_0 \mu_0)^{1/2}]$, whose amplitudes and phases depend on the expansion coefficients of internal field A_{mn} and B_{mn} , respectively [41].

$$\mathbf{E}^{int} = \sum_{n=1}^{\infty} \sum_{m=-n}^{n} [A_{mn} \mathbf{M}_{mn}^{(1)}(\mathbf{r}, k_1) + A_{mn} \mathbf{N}_{mn}^{(1)}(\mathbf{r}, k_1) + B_{mn} \mathbf{M}_{mn}^{(1)}(\mathbf{r}, k_2) - B_{mn} \mathbf{N}_{mn}^{(1)}(\mathbf{r}, k_2)],$$
(17)

$$\mathbf{H}^{int} = Q \sum_{n=1}^{\infty} \sum_{m=-n}^{n} [A_{mn} \mathbf{M}_{mn}^{(1)}(\mathbf{r}, k_1) + A_{mn} \mathbf{N}_{mn}^{(1)}(\mathbf{r}, k_1) - B_{mn} \mathbf{M}_{mn}^{(1)}(\mathbf{r}, k_2) + B_{mn} \mathbf{N}_{mn}^{(1)}(\mathbf{r}, k_2)].$$
(18)

Here $Q = -i(\varepsilon_c/\mu_c)^{1/2}$. For a chiral spherical particle with radius a, the size parameters are defined as $x_0 = k_0 a$, $x_1 = k_1 a$ and $x_2 = k_2 a$. In terms of which the expressions for A_n^{sa} , A_n^{sb} , B_n^{sa}

and B_n^{sb} are given as follows:

$$A_n^{Sa} = \frac{\Psi_n(x_0)}{\xi_n(x_0)} \frac{\frac{D_n^{(1)}(x_1) - \eta_r D_n^{(1)}(x_0)}{\eta_r D_n^{(1)}(x_1) - D_n^{(3)}(x_0)} + \frac{D_n^{(1)}(x_2) - \eta_r D_n^{(1)}(x_0)}{\eta_r D_n^{(1)}(x_2) - D_n^{(3)}(x_0)}}{\frac{\eta_r D_n^{(3)}(x_0) - D_n^{(1)}(x_1)}{\eta_r D_n^{(1)}(x_1) - D_n^{(3)}(x_0)} + \frac{\eta_r D_n^{(3)}(x_0) - D_n^{(1)}(x_2)}{\eta_r D_n^{(1)}(x_2) - D_n^{(3)}(x_0)}},$$
(19)

$$A_n^{sb} = \frac{\Psi_n(x_0)}{\xi_n(x_0)} \frac{\frac{\eta_r D_n^{(1)}(x_1) - D_n^{(1)}(x_0)}{\eta_r D_n^{(1)}(x_1) - D_n^{(3)}(x_0)} - \frac{\eta_r D_n^{(1)}(x_2) - D_n^{(1)}(x_0)}{\eta_r D_n^{(1)}(x_2) - D_n^{(3)}(x_0)}}{\frac{\eta_r D_n^{(3)}(x_0) - D_n^{(1)}(x_1)}{\eta_r D_n^{(1)}(x_1) - D_n^{(3)}(x_0)} + \frac{\eta_r D_n^{(3)}(x_0) - D_n^{(1)}(x_2)}{\eta_r D_n^{(1)}(x_2) - D_n^{(3)}(x_0)}},$$
(20)

$$B_n^{sa} = \frac{\Psi_n(x_0)}{\xi_n(x_0)} \frac{\frac{\eta_r D_n^{(1)}(x_1) - D_n^{(1)}(x_0)}{\eta_r D_n^{(1)}(x_1) - D_n^{(3)}(x_0)} - \frac{\eta_r D_n^{(1)}(x_2) - D_n^{(1)}(x_0)}{\eta_r D_n^{(1)}(x_2) - D_n^{(3)}(x_0)}}{\frac{\eta_r D_n^{(3)}(x_0) - D_n^{(1)}(x_1)}{\eta_r D_n^{(1)}(x_1) - D_n^{(3)}(x_0)} + \frac{\eta_r D_n^{(3)}(x_0) - D_n^{(1)}(x_2)}{\eta_r D_n^{(1)}(x_2) - D_n^{(3)}(x_0)}},$$
(21)

$$B_n^{sb} = \frac{\Psi_n(x_0)}{\xi_n(x_0)} \frac{\frac{\eta_r D_n^{(1)}(x_1) - D_n^{(1)}(x_0)}{D_n^{(1)}(x_1) - \eta_r D_n^{(3)}(x_0)} + \frac{\eta_r D_n^{(1)}(x_2) - D_n^{(1)}(x_0)}{D_n^{(1)}(x_2) - \eta_r D_n^{(3)}(x_0)}}{\frac{D_n^{(3)}(x_0) - \eta_r D_n^{(1)}(x_1)}{D_n^{(1)}(x_1) - \eta_r D_n^{(3)}(x_0)} + \frac{D_n^{(3)}(x_0) - \eta_r D_n^{(1)}(x_2)}{D_n^{(1)}(x_2) - \eta_r D_n^{(3)}(x_0)}}.$$
(22)

In these equations, $\eta_r = \sqrt{\varepsilon_0/\mu_0} / \sqrt{\varepsilon_c/\mu_c}$. $\Psi_n(x) = xj_n(x)$ and $\xi_n(x) = xh_n^{(1)}(x)$ are the first kind and third kind Riccati-Bessel functions, in terms of which the logarithmic derivatives $D_n^{(1)}(x) = \Psi_n'(x) / \Psi_n(x)$ and $D_n^{(3)}(x) = \xi_n'(x) / \xi_n(x)$ can be defined. For a given polarization of the incident wave, the expansion coefficients of the incident field take a different form. For example, for a linear polarized wave, i.e., an *x*-polarized wave propagating along the *z*-axis with the field $\mathbf{E}^{ix} = E_0 e^{ikz} \hat{x}$, the expansion coefficients are given as follows:

$$a_{mn}^{ix} = \begin{cases} i^{n+1} \frac{2n+1}{2n(n+1)} & m=1\\ i^{n+1} \frac{2n+1}{2} & m=-1, \end{cases}$$
 (23)

$$b_{mn}^{ix} = \begin{cases} i^{n+1} \frac{2n+1}{2n(n+1)} & m = 1\\ -i^{n+1} \frac{2n+1}{2} & m = -1. \end{cases}$$
 (24)

The above expansion coefficients a_{mn}^{ix} and b_{mn}^{ix} vanish for $m \neq \pm 1$. For they-polarized incident wave, the expansion coefficients are related to a_{mn}^{ix} and b_{mn}^{ix} through $a_{mn}^{iy} = -ib_{mn}^{ix}$ and $b_{mn}^{iy} = -ia_{mn}^{ix}$.

Appendix B

By calculating the corresponding components of the Poynting vector of the scattered field and using the definition Δ_{SH} in Eq. (6), the following relation for PSHS in terms of scattering coefficients can be obtained [36].

$$\Delta_{\text{SH}} = -\frac{\sqrt{2}\sigma\sin\theta}{k} \frac{Re\left[\sum_{n=1}^{\infty}\sum_{m=-n}^{n} C_n((-1)^{n+1}B_{mn}^s\pi_{mn} \cdot S_1^* + \sigma S_2 \cdot (A_{mn}^s\pi_{mn})^*)\right]}{|S_2|^2 + |S_1|^2},$$
 (25)

where $\sigma = \pm 1$ corresponds to the helicity of the incident wave, $C_n = n(n+1)(i)^{n+1}$, S_1 and S_2 are the scattering matrix amplitudes, which are given as

$$S_1 = \sigma \sqrt{2} \sum_{n=1}^{\infty} \sum_{m=-n}^{n} (-i)^{n+1} \left(A_{mn}^s \tau_{mn} + m \cdot B_{mn}^s \pi_{mn} \right), \tag{26}$$

$$S_2 = \sqrt{2} \sum_{n=1}^{\infty} \sum_{m=-n}^{n} (-i)^{n+1} \left(B_{mn}^s \tau_{mn} + m \cdot A_{mn}^s \pi_{mn} \right). \tag{27}$$

Here, π_{mn} and τ_{mn} are defined as $P_n^m/\sin(\theta)$ and $dP_n^m/d\theta$, respectively, where P_n^m is the associated Legendre function. For a spherical scatterer, the far-field intensity is given as.

$$I(\theta) = \lim_{r \to \infty} k^2 r^2 \left| E_{\theta}^s E_{\theta}^{s*} + E_{\varphi}^s E_{\varphi}^{s*} \right| = \frac{E_0^2}{2} \left(|S_2|^2 + |S_1|^2 \right). \tag{28}$$

The above relation can be used together with Eq. (25) to express the PSHS in terms of the far-field scattering intensity, as given in Eq. (8). Due to the intrinsic chirality of the particle, both the PSHS and the scattering intensity can be optimized by matching the handedness of the incident wave and the chiral particle. The corresponding results of PSHS and the scattering intensity for the LCP incident wave can be obtained from Eq. (25) and Eq. (28) while using the scattering coefficients given in Eq. (5) instead of Eq. (4). Similarly, the duality of the particle can be evaluated by using the following transfer function.

$$T = \frac{w_{-p}^{sca}}{w_p^{sca}} = \frac{\sum_{n=1}^{\infty} \frac{1}{2n+1} \left| A_{-1n}^s + B_{-1n}^s \right|^2}{\sum_{n=1}^{\infty} \frac{1}{2n+1} \left| B_{-1n}^s - A_{-1n}^s \right|^2}.$$
 (29)

Funding. National Key R& D Program of China (2022YFA1404301); National Natural Science Foundation of China (12174281, 12311530763, 12274314); Natural Science Foundation of Jiangsu Province (BK20221240); Suzhou Basic Research Project (SJC2023003).

Disclosures. The authors declare no conflicts of interest.

Data availability. The codes and data underlying the results presented in this paper are not publicly available at this time but may be obtained from the authors upon reasonable request.

References

- K. Y. Bliokh, F. J. Rodríguez-Fortu no, F. Nori, et al., "Spin-orbit interactions of light," Nat. Photonics 9(12), 796–808 (2015).
- 2. K. Y. Bliokh, E. A. Ostrovskaya, M. A. Alonso, *et al.*, "Spin-to-orbital angular momentum conversion in focusing, scattering, and imaging systems," Opt. Express **19**(27), 26132 (2011).
- L. T. Vuong, A. J. L. Adam, J. M. Brok, et al., "Electromagnetic spin-orbit interactions via scattering of subwavelength apertures," Phys. Rev. Lett. 104(8), 083903 (2010).
- C. Imbert, "Calculation and experimental proof of the transverse shift induced by total internal reflection of a circularly polarized light beam," Phys. Rev. D 5(4), 787–796 (1972).
- 5. M. Onoda, S. Murakami, and N. Nagaosa, "Hall effect of light," Phys. Rev. Lett. 93(8), 083901 (2004).
- C. Mi, S. Chen, W. Wu, et al., "Precise identification of graphene layers at the air-prism interface via a pseudo-Brewster angle," Opt. Lett. 42(20), 4135 (2017).
- P. Tang, X. Li, Y. Kim, et al., "Spin Hall Effect of Light in a Dichroic Polarizer for Multifunctional Edge Detection," ACS Photonics 11(10), 4170 (2024).
- P. Tang, Y. Kim, T. Badloe, et al., "Polarization-independent edge detection based on the spin-orbit interaction of light," Opt. Express 32(10), 17560 (2024).
- 9. W. J. M. Kort-Kamp, "Topological phase transitions in the photonic spin Hall effect," Phys. Rev. Lett. **119**(14), 147401 (2017)
- 10. J. Zhou, H. Qian, G. Hu, et al., "Broadband photonic spin Hall meta-lens," ACS Nano 12(1), 82-88 (2018).
- 11. K. Y. Bliokh, A. Niv, V. Kleiner, et al., "Geometrodynamics of spinning light," Nat. Photonics 2(12), 748-753 (2008).
- J. Choi, S. Shim, Y. Kim, et al., "Experimental observation of spin Hall effect of light using compact weak measurements," Nanophotonics 13(20), 3877–3882 (2024).
- X. Ling, X. Zhou, K. Huang, et al., "Recent advances in the spin Hall effect of light," Rep. Prog. Phys. 80(6), 066401 (2017).
- O. Hosten and P. Kwiat, "Observation of the spin Hall effect of light via weak measurements," Science 319(5864), 787–790 (2008).
- O. G. Rodríguez-Herrera, D. Lara, K. Y. Bliokh, et al., "Optical nanoprobing via spin-orbit interaction of light," Phys Rev. Lett. 104(25), 253601 (2010).
- A. He, Y. Xu, B. Gao, et al., "Subwavelength broadband photonic spin Hall devices via optical slot antennas," Laser Photonics Rev. 15(5), 2000460 (2021).

- 17. X. Zhou, X. Lin, Z. Xiao, *et al.*, "Controlling photonic spin Hall effect via exceptional points," Phys. Rev. B **100**(11), 115429 (2019).
- R. Ali, T. P. M. Alegre, and G. S. Wiederhecker, "Enhancing the Goos-Hänchen and spin-Hall shifts in planar and spherical structures through complex-frequency excitations," Phys. Rev. B 110(8), 085403 (2024).
- M. Shah, M. S. Anwar, R. Asgari, et al., "Photonic spin Hall effect in Haldane model materials," Phys. Rev. B 109(23), 235418 (2024).
- S. Li, X. Li, G. Wang, et al., "Multidimensional manipulation of photonic spin Hall effect with a single-layer dielectric metasurface," Adv. Opt. Mater. 7(5), 1801365 (2019).
- 21. X. Ling, W. Xiao, S. Chen, *et al.*, "Revisiting the anomalous spin-Hall effect of light near the Brewster angle," Phys. Rev. A **103**(3), 033515 (2021).
- 22. W. Yang, L. K. Ang, W. Zhang, *et al.*, "High sensitivity gas sensor based on surface exciton polariton enhanced photonic spin Hall effect," Opt. Express **31**(16), 27041 (2023).
- 23. M. Kim, Y. Yang, D. Lee, *et al.*, "Spin Hall effect of light: from fundamentals to recent advancements," Laser Photonics Rev. **17**(1), 2200046 (2023).
- M. Kim, D. Lee, Y. Yang, et al., "Reaching the highest efficiency of spin Hall effect of light in the near-infrared using all-dielectric metasurfaces," Nat. Commun. 24, 29771 (2022).
- W. Luo, S. Xiao, Q. He, et al., "Photonic spin Hall effect with nearly 100% efficiency," Adv. Opt. Mater. 3(8), 1102–1108 (2015).
- 26. Y. Kim, X. Li, P. Tang, et al., "Spin-Dependent Phenomena of Meta-optics," ACS Photonics 12(1), 16–33 (2025).
- D. Haefner, S. Sukhov, and A. Dogariu, "Spin Hall effect of light in spherical geometry," Phys. Rev. Lett. 102(12), 123903 (2009).
- D. Gao, R. Shi, A. E. Miroshnichenko, et al., "Enhanced spin Hall effect of light in spheres with dual symmetry," Laser Photonics Rev. 12(11), 1800130 (2018).
- J. Olmos-Trigo, C. Sanz-Fernández, A. García-Etxarri, et al., "Enhanced spin-orbit optical mirages from dual nanospheres," Phys. Rev. A 99(1), 013852 (2019).
- J. Lasa-Alonso, J. Olmos-Trigo, A. García-Etxarri, et al., "Correlations between helicity and optical losses within general electromagnetic scattering theory," Mater. Adv. 3(10), 4179

 –4185 (2022).
- Y. Sun, P. Xu, L. Gao, et al., "Wavelength-scale spin Hall shift of light with morphology-enhanced scattering efficiency from nanoparticles," Laser Photonics Rev. 16(11), 2200289 (2022).
- 32. J. Mun, M. Kim, Y. Yang, et al., "Electromagnetic chirality: from fundamentals to nontraditional chiroptical phenomena," Light: Sci. Appl. 9(1), 139 (2020).
- 33. P. Spaeth, S. Adhikari, L. Le, *et al.*, "Circular dichroism measurement of single metal nanoparticles using photothermal imaging," Nano Lett. **19**(12), 8934–8940 (2019).
- 34. I. Fernandez-Corbaton, M. Fruhnert, and C. Rockstuhl, "Objects of maximum electromagnetic chirality," Phys. Rev. X 6(3), 031013 (2016).
- J. Ni, Shunli Liu, Y. Chen, et al., "Direct observation of spin-orbit interaction of light via chiroptical responses," Nano Lett. 22(22), 9013–9019 (2022).
- R. Ali, "Chirality-assisted spin Hall effect of light in the vicinity of the quasi-antidual symmetry mode of a chiral sphere," Phys. Rev. A 106(6), 063508 (2022).
- 37. X. Zambrana-Puyalto, I. Fernandez-Corbaton, M. L. Juan, et al., "Duality symmetry and Kerker conditions," Opt. Lett. 38(11), 1857 (2013).
- 38. A. Lakhtakia, Beltrami fields in chiral media, (World Scientific, 1994), Vol. 2.
- 39. C. F. Bohren, "Light scattering by an optically active sphere," Chem. Phys. Lett. 29(3), 458-462 (1974).
- 40. Q. C. Shang, Z. S. Wu, T. Qu, et al., "Analysis of rainbow scattering by a chiral sphere," Opt. Express 21(19), 21879 (2013).
- 41. Z. S. Wu, Q. C. Shang, and Z. J. Li, "Calculation of electromagnetic scattering by a large chiral sphere," Appl. Opt. 51(27), 6661 (2012).
- J. Olmos-Trigo, C. Sanz-Fernández, D. R. Abujetas, et al., "Optical mirages from spinless beams," ACS Photonics 10(6), 1742–1747 (2023).
- K. Y. Bliokh and A. Aiello, "Goos-Hänchen and Imbert-Fedorov beam shifts: an overview," J. Opt. 15(1), 014001 (2013).
- 44. Q.-C. Shang, Z.-S. Wu, T. Qu, *et al.*, "Analysis of the radiation force and torque exerted on a chiral sphere by a Gaussian beam," Opt. Express **21**(7), 8677 (2013).
- 45. J. Soni, S. Mansha, S. Dutta Gupta, *et al.*, "Giant Goos-Hänchen shift in scattering: the role of interfering localized plasmon modes," Opt. Lett. **39**(14), 4100 (2014).
- J. Olmos-Trigo, M. Nieto-Vesperinas, and G. Molina-Terriza, "Spheres of maximum electromagnetic chirality," Phys. Rev. Res. 6(4), 043192 (2024).
- 47. X. Zambrana-Puyalto, X. Vidal, M. L. Juan, *et al.*, "Dual and anti-dual modes in dielectric spheres," Opt. Express **21**(15), 17520 (2013).
- J. Olmos-Trigo, D. R. Abujetas, C. Sanz-Fernández, et al., "Optimal backward light scattering by dipolar particles," Phys. Rev. Res. 2(1), 013225 (2020).
- J. Soni, S. Ghosh, S. Mansha, et al., "Enhancing spin-orbit interaction of light by plasmonic nanostructures," Opt. Lett. 38(10), 1748 (2013).

- 50. D. Pan, H. Wei, L. Gao, *et al.*, "Strong spin-orbit interaction of light in plasmonic nanostructures and nanocircuits," Phys. Rev. Lett. **117**(16), 166803 (2016).
- 51. E. Mignani, E. Recami, and M. Baldo, "About a Dirac-like equation for the photon according to Ettore Majorana," Lett. Nuovo Cimento 11(12), 568–572 (1974).
- 52. K. Y. Bliokh, A. Y. Bekshaev, and F. Nori, "Extraordinary momentum and spin in evanescent waves," Nat. Commun. 5(1), 3300 (2014).
- 53. C. Triolo, A. Cacciola, S. Patanè, *et al.*, "Spin-momentum locking in the near field of metal nanoparticles," ACS Photonics **4**(9), 2242–2249 (2017).
- 54. X. Ling, X. Zhou, X. Yi, et al., "Giant photonic spin Hall effect in momentum space in a structured metamaterial with spatially varying birefringence," Light: Sci. Appl. 4(5), e290 (2015).